# Rainfall Characteristics and their Environmental Conditions during the Heavy Rainfall Events over Japan in July of 2017 and 2018

**Takashi UNUMA**

*Observation Department, Japan Meteorological Agency, Tokyo, Japan*

**and**

**Tetsuya TAKEMI**

*Disaster Prevention Research Institute, Kyoto University, Kyoto, Japan*

## Abstract

In July of 2017 and 2018, heavy rainfall events occurred, leading to significant damage in Japan. This study investigated the rainfall characteristics and environmental conditions for these heavy rainfall events using rain intensity data from operational weather radars and mesoscale analysis data. An automatic algorithm was developed to categorize precipitating cloud systems into five types, one with weaker rainfall (less than 10 mm h$^{-1}$) and four with stronger rainfall (greater than or equal to 10 mm h$^{-1}$), i.e., quasi-stationary convective clusters (QSCCs), propagating convective clusters (PCCs), short-lived convective clusters (SLCC), and other convective but unorganized rainfall. The rainfall amount due to the weaker rainfall was found to dominate the total rainfall in most of the analysis region; however, the contribution from the stronger rainfall types became larger than that from the weaker rainfall type in regions that experienced heavy rainfall. Among the stronger rain types, SLCCs dominate over the rainfall contributions from QSCCs or PCCs, whereas rainfalls from convective but unorganized systems are very minor. It was emphasized that the contribution from stronger rains due to organized systems with areas of 200 km$^2$ plays a major role in regions with significant amounts of rainfall during the heavy rainfall events examined here. The examination of the environmental conditions for the development of each system demonstrated that, from the viewpoint of moisture content, the stability conditions were more unstable in 2018 than in 2017. There is also a clear linkage in the time series between rainfall types and the environmental properties of precipitable water and vertical shear. It was found that both the column moisture content and the middle-to-upper-level relative humidity characterize the environmental conditions for the occurrence of the present heavy rainfall events. Features of the rainfall types and their environmental conditions were compared with the QSCC climatology.

**Keywords**   heavy rainfall; environmental properties; mesoscale convective systems; precipitating cloud systems; extreme rainfall in July 2017 and 2018

---

Corresponding author: Tetsuya Takemi, Disaster Prevention Research Institute, Kyoto University, Gokasho, Uji, Kyoto 611-0011, Japan
E-mail: takemi@storm.dpri.kyoto-u.ac.jp

## 1. Introduction

Heavy rainfall is responsible for many societal impacts such as flash floods, inundations, and landslides. Heavy rains are known to occur frequently during the Baiu season in Japan (e.g., Tsuguti and Kato 2014), and there have been cases causing severe damage in recent years. In July 2017, heavy rainfall caused by a long-lasting, linear-shaped rainfall system in the northern part of Kyushu Island produced a total rainfall amount in one area that exceeded 600 mm within 9 hours (Kato et al. 2018; Takemi 2018). In July 2018, widespread heavy rainfall events occurred over Japan, particularly in the western and central parts of the country, causing a large number of fatalities and serious damage across extensive areas (Cabinet Office 2019; Tsuguti et al. 2019). The casualties from the July 2018 event exceeded 240, making it one of the worst meteorological disasters in the past three decades. Understanding the behavior of extreme-rain-producing cloud systems and their environmental properties is important for better predicting extreme rainfall events caused by such convective systems.

Because of its significant effects, a number of recent studies have investigated the July 2018 Heavy Rainfall event. Shimpo et al. (2019) examined large-scale atmospheric conditions for the extreme rainfall event in July 2018 and the subsequent heat wave in Japan to demonstrate that persistent moist airflows associated with Baiu frontal ascent provided conditions favorable for the occurrence of the extreme rainfall and that the western North Pacific Subtropical High and the upper-level Tibetan High jointly enhanced hot weather in summer 2018. Sekizawa et al. (2019) highlighted the role of anomalous moisture transport from the ocean to northern Kyushu Island in forming the rainfall systems in July 2018. The role of strong southerly moisture flux in causing the extreme rainfall event of July 2018 was also investigated by Takemura et al. (2019), who showed that the extreme rainfall could be attributed to two branches of extremely moist inflow, i.e., a shallow southerly airflow from the North Pacific Subtropical High and a deep southwesterly airflow from active convection over the East China Sea. These studies demonstrate the importance of moist airflow toward the Japanese islands.

With the above large-scale conditions in mind, Takemi and Unuma (2019) diagnosed the environmental properties surrounding the convective systems that generated the heavy rainfall event in July 2018 and found that higher relative humidity in the middle-to-upper troposphere provides favorable conditions for the development of convective systems. The importance of humid middle-level conditions in generating and enhancing convective systems has been recognized in the tropics (Derbyshire et al. 2004; Kikuchi and Takayabu 2004; Takemi et al. 2004; Takemi 2015) as well as in midlatitudes (Takemi 2006, 2007a; Unuma and Takemi 2016a, hereafter referred to as UT16a; Yokoyama et al. 2017; Hamada and Takayabu 2018). In an extreme rainfall event over eastern Japan in October 2019, middle-level humid conditions were identified as a major factor in generating the rainfall systems (Takemi and Unuma 2020). Thus, middle-level humidity in the July 2017 and 2018 cases are of interest in further studies.

In addition, Takemi and Unuma (2019) used operational radar data to extract stationary or slow-moving meso-β-scale convective systems known as quasi-stationary convective clusters (QSCCs) (UT16a; Unuma and Takemi 2016b) and found that QSCCs appeared to have a minor effect in producing the July 2018 heavy rainfall. It was suggested that systems with weaker precipitation intensity or faster speed had greater effects on the total amount of rainfall in the July 2018 case. Therefore, the other systems that are not categorized as QSCCs should be examined to gain a full picture of what types of rainfall systems contributed to the total rainfall amount in this event.

Sueki and Kajikawa (2019) examined rainfall types for the July 2018 case in terms of precipitating area using operational radar data. They categorized rainfall into five types based on the intensity and area of precipitation, and found that a rainfall type with a rainfall area of greater than or equal to $10^4$ km$^2$ was generated mainly in areas with the heaviest rainfall. Additionally, they suggested that faster-moving systems under a strong low-level shear environment may have affected the July 2018 heavy rainfall event. Takemi and Unuma (2019) also identified the existence of faster-moving systems in this case. However, there are still unknown aspects of rainfall characteristics, types of rain-producing cloud systems, and the environmental conditions for the development of such rainfall systems. At present, few studies have been conducted using a statistical approach as was used in UT16a. Most studies chose some specific case, documented its features in detail, and investigated causes for the development of that case. In contrast to such case-based studies, we try to reveal general characteristics commonly seen in rain-producing systems during extreme events using a statistical approach. Such statistical treatment of multiple convective systems that occur during the heavy rainfall events for a given case has never done before,
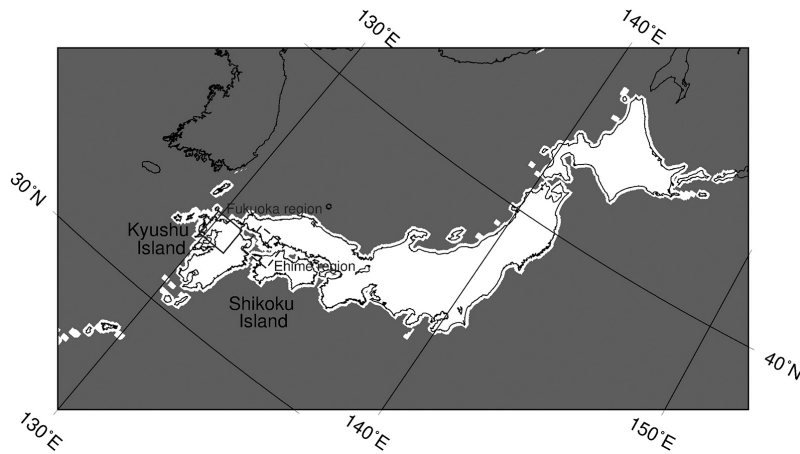
Fig. 1. The analysis area used in this study. Rectangles with solid and dashed lines indicate the Fukuoka and Ehime regions, respectively.

making this a unique approach in this study.

The purpose of this study is to investigate and document types of rainfall and precipitating cloud systems that produced the July 2017 and 2018 heavy rainfall events and the environmental conditions involved in the development of such convective systems. We extend UT16a's algorithm to detect QSCCs and faster-moving convective clusters by updating the convective cluster tracking procedure in UT16a and compare the heavy rainfall events in July of 2017 and 2018. We also investigate the environmental conditions that would distinguish rainfall types by examining stability and shear conditions.

## 2. Data and analysis overview

Rainfall characteristics were investigated with the use of rain intensity data obtained by Japan Meteorological Agency (JMA) weather radars. The data have the spatial resolution of 1 km and a 10-minute interval, recorded in the unit of mm h$^{-1}$. The radar data coverage used in this study is shown in Fig. 1. As in UT16a, we used data over land or coastal seas within 10 km of the coastline to focus on the activity of precipitating systems over most of the Japanese islands.

The radar data were used to extract mesoscale convective systems. First, we identified QSCCs, as found in UT16a and defined as a stationary or slowly moving cluster of convective cells with a horizontal size in meso-β-scales and a shape that is mostly linearly elongated (Unuma and Takemi 2016b). In UT16a, the motion speed of a QSCC is limited to 10 m s$^{-1}$, and this study followed their methods to identify QSCCs.

In addition, we included propagating convective systems by extending the algorithm of UT16a and considering systems with motion speeds exceeding 10 m s$^{-1}$, thereby classifying convective clusters (CCs) into different precipitation features. We defined propagating CCs (PCCs), which moved faster than QSCCs, and further categorized rainfall types that were not identified as either QSCCs or PCCs.

In this study, we made some modifications to the procedure for selecting CCs at their initial times, enabling us to increase the number of CCs tracked as QSCCs or PCCs. When determining the initial time of CCs for tracking, the algorithm of UT16a imposes two restrictions: search range and overlapping ratio. After examination, we found that the overlapping ratio restriction strongly limited the number of CC detections. Therefore, the overlap ratio restriction was excluded when determining the initial time of CCs for tracking; hence, the CC initial time was determined using only the search range restriction. The procedure to extract PCCs and QSCCs will be further explained in Section 3.1.

To diagnose the environmental conditions for the heavy rainfall events of July 2017 and 2018, we used the analysis fields (known as mesoscale analysis, Japan Meteorological Agency 2013; hereafter MA) from the Mesoscale Model (MSM) of the JMA (Saito et al. 2006). The MA data are available with a horizontal resolution of 5 km and a time interval of 3 h. With the use of MA data, some of the environmental indices and parameters generally used for mesoscale analyses were examined this study. The heavy rainfall events targeted in this study are those that caused heavy rainfall events within the span of a few hours in

limited areas and those that lasted several days over wider areas. Although the time and spatial scales are quite different, heavy rainfall events occur in a certain place. To understand the characteristics of the heavy rainfall events, we examined properties of the environmental conditions before the occurrence of precipitating systems at a certain place as in UT16a. Following the studies of Chuda and Niino (2005), Nomura and Takemi (2011), Takemi (2014a), and UT16a, we used convective available potential energy (CAPE), convective inhibition (CIN), precipitable water (PW), Showalter stability index (SSI), K index (KI; George 1960), temperature lapse late from 850 and 500 hPa (TLR; Takemi 2007a, b, 2010, 2014b), 0–3 km mean shear (MS03; Rasmussen and Blanchard 1998), and 0–3 km environmental helicity (EH03; Davies-Jones 1984). CAPE is calculated by adiabatically raising a parcel with properties that are vertically averaged in the lowest 500 m layer. In addition, we examined mean shear averaged vertically in the troposphere between 1000 hPa and 300 hPa (MStr).

The analysis time period was one week for the 2017 and 2018 events. The period chosen for the 2017 event was from 0000 Japan Standard Time (JST) 30 June to 0000 JST 7 July. For the 2018 event, the period was from 0000 JST 2 July to 0000 JST 9 July. All times herein are in JST, which is UTC+9. The reason for setting the analysis period to one week is to compare heavy rainfall events with different spatiotemporal scales on a fixed scale and using the same analysis method.

To demonstrate the overall features of the heavy rainfall events, we first demonstrate the total amount of rainfall from the radar/raingauge analyzed rainfall data (Nagata 2011), during the analysis time periods for the 2017 and 2018 cases (Fig. 2). The maximum value among the total rainfall amounts in each 50 km by 50 km area is shown in Fig. 2 (see Supplement 3 for the original 1 km resolution data). In the July 2017 case, extreme rainfalls exceeding 600 mm are seen in the northern part of Kyushu and in some coastal areas of the Sea of Japan. In the 2018 case, the extreme rainfalls are widely spread in the western and central parts of Japan. In later sections, we will investigate the rainfall characteristics and environmental properties over Japan during the analysis time periods. In examining the environmental properties for the development of rainfall systems, we will not only investigate the conditions over the Japanese main islands but also focus on two specific regions with larger amounts of rainfall, i.e., the Fukuoka and Ehime regions, which are at almost the same latitude and have relatively
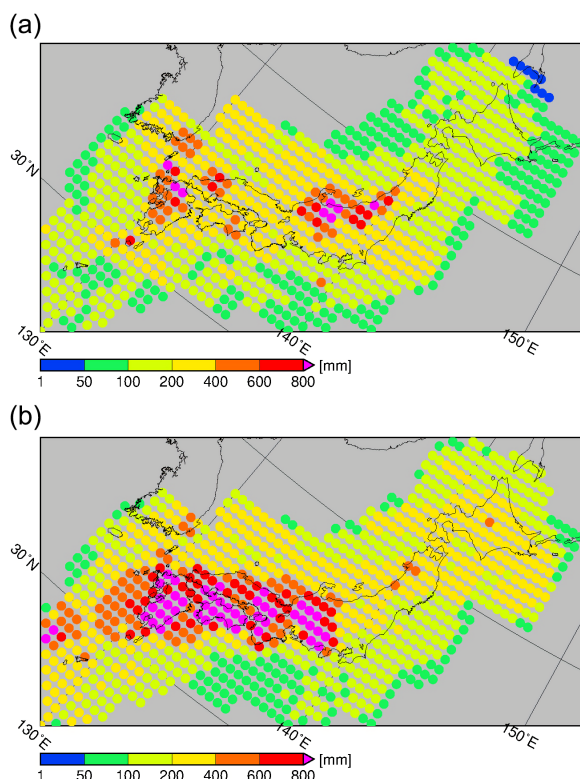


Fig. 2. Accumulated rainfall amounts shown in terms of the maximum value in each 50 km by 50 km area (a) from 0000 JST 30 June to 0000 JST 7 July 2017 and (b) from 0000 JST 2 July to 0000 JST 9 July 2018.

similar climatic characteristics, to compare rainfall features between the 2017 and 2018 cases using an identical analysis method.

## 3. Rainfall characteristics

### 3.1 Convective clusters

In this section, we extract quasi-stationary or propagating mesoscale convective systems, i.e., QSCCs and PCCs, from the radar data and demonstrate the general features of QSCCs and PCCs.

First, we identify CCs at each time step using the procedure of UT16a. A CC is defined as having a contiguous region of intense precipitation (i.e., greater than or equal to 10 mm h$^{-1}$) with an area of 200 km$^2$ or greater. The motion speed was then computed by searching the centroids of the detected CCs at two time steps (one time step is equal to a 10 minute interval), and the range of this search is limited to a 10 km radius. In UT16a, they set a maximum threshold of motion speed to 10 m s$^{-1}$ to extract QSCCs. We did
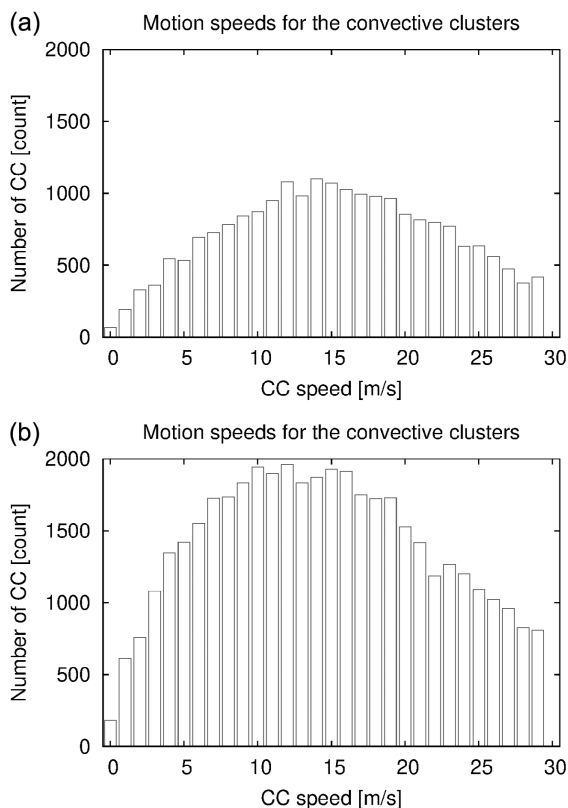
(a)

Motion speeds for the convective clusters



(b)

Motion speeds for the convective clusters



Fig. 3. Frequency distributions of convective cluster speeds in the (a) 2017 heavy rainfall case and the (b) 2018 heavy rainfall case.

(a)



(b)



Fig. 4. The spatial distribution of the number of detection of (a) QSCCs and (b) PCCs evaluated over 50 km by 50 km areas for the 2017 heavy rainfall case.

not initially set a motion speed threshold in this study, but rather examined the features of the motion speeds of CCs to distinguish QSCCs and PCCs.

Figure 3 shows frequency distributions of the motion speed of the detected CCs in the 2017 and 2018 cases. The 2017 case shows a peak at approximately, but slightly higher than, 10 m s$^{-1}$. The 2018 case also shows a peak at around 10 m s$^{-1}$. The total number of detected CCs in 2018 is about two times larger than in 2017, and both cases appear to have normal distributions despite a slight shift toward higher values in 2017. From the distributions of the 2017 and 2018 cases, it seems reasonable to set the threshold speed separating stationary/slow-moving and propagating CCs at 10 m s$^{-1}$, the value used to detect QSCCs in UT16a.

From this analysis, here we identify QSCCs and PCCs. The motion speed of CCs is defined as the temporal mean speed averaged over the CC's lifetime. If the time-mean motion speed is less than (greater than
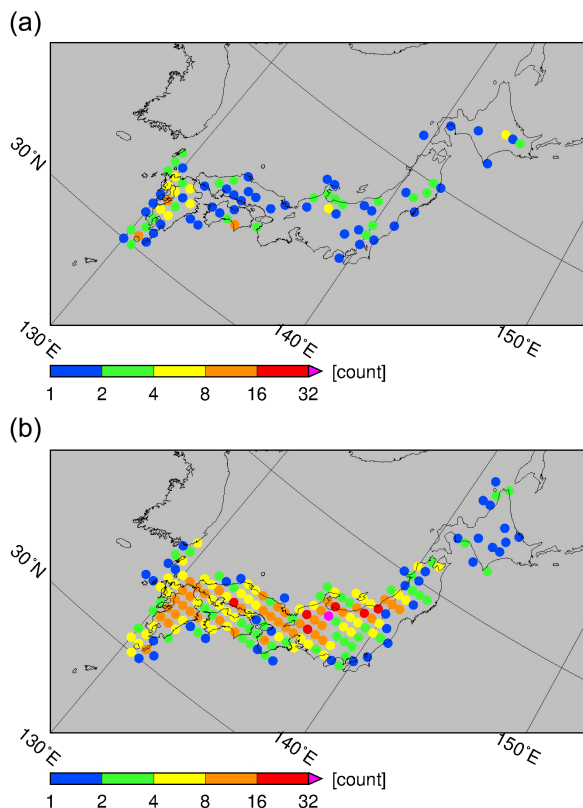
or equal to) 10 m s$^{-1}$, the detected CC is then categorized as a QSCC (PCC). As mentioned in Section 2.2 of UT16a, the minimum lifetime was set to 20 minutes, which means that identical QSCCs or PCCs must be tracked for at least three time steps. In other words, in the current procedure, there are organized and short-lived systems that are not categorized as either QSCCs or PCCs. We defined such systems as short-lived convective clusters (SLCCs), the characteristics of which will be mentioned in the next subsection. In this subsection, we will describe QSCC and PCC features in terms of their frequency distributions and lifetimes.

The development of QSCCs and PCCs in the 2017 case is demonstrated in Fig. 4. As in UT16a, the number of QSCC and PCC occurrences is summed up in each 50 km by 50 km area, yielding 185 QSCCs and 1041 PCCs. Both QSCCs and PCCs are widely distributed over the heavy rainfall regions shown in Fig. 2a. It should be noted that the frequency of
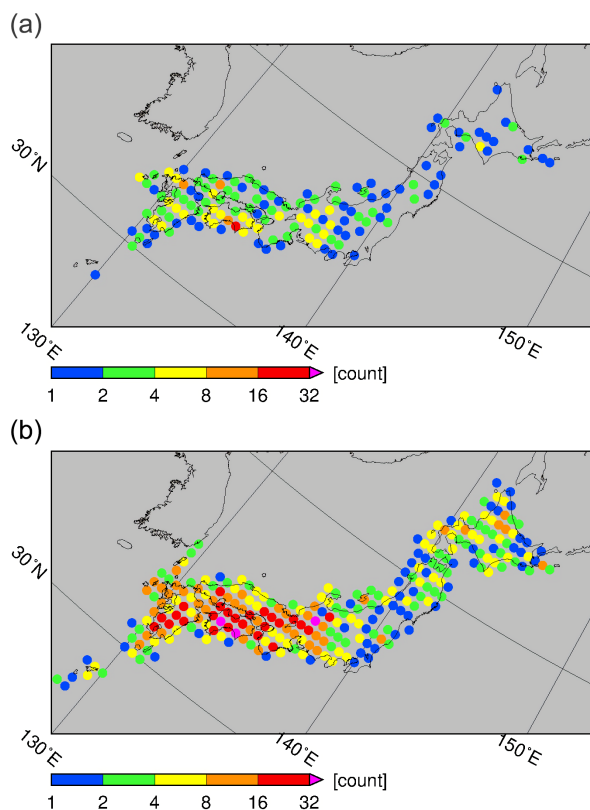
(a)



(b)



Fig. 5.   The same as Fig. 4, except for the 2018 heavy rainfall case.
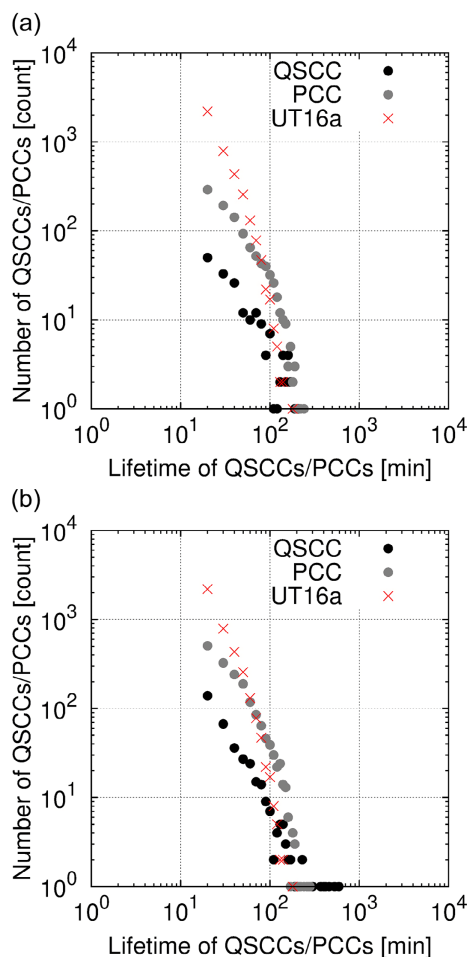
(a)



(b)



Fig. 6.   Number of QSCCs (black dot) and PCCs (gray dot) versus lifetime, counted at 10-minute intervals in (a) the 2017 case and (b) the 2018 case. The number of QSCCs in UT16a (red crosses) is also shown for reference.

QSCCs is high in the northern part of Kyushu, which corresponds to the July 2017 Northern Kyushu Heavy Rainfall event (Kato et al. 2018; Takemi 2018). Compared to the QSCCs appearance, PCCs are more widely spread.

Figure 5 shows the spatial distribution of QSCCs and PCCs in the 2018 case. The total numbers of QSCCs and PCCs are 375 and 1737, respectively. Again, QSCCs and PCCs appear in regions with heavy rainfall (see Fig. 2b). QSCCs develop more frequently in the western part of Japan, especially in the Shikoku and Kyushu regions.

The features of QSCCs and PCCs are demonstrated in terms of their lifetimes. Figure 6 shows the distributions of QSCC and PCC lifetimes. The mean/median QSCC values in the 2017 (2018) cases are 56/40 (55/30) minutes and the PCC values are 50/40 (47/40) minutes. The lifetimes of QSCCs and PCCs appear to be longer in 2017 than in 2018. Compared to the statistics of the QSCC lifetimes identified in UT16a, the number of occurrences with shorter lifetimes appears to be relatively small. This is probably because the

2017 and 2018 cases have smaller numbers of samples than the statistical analysis of UT16a. The number of QSCCs (PCCs) with lifetimes longer than 200 (90) minutes is greater in the 2017 and 2018 cases than in UT16a, which is mainly due to the modifications to the CC tracking procedure in UT16a. The shape of the lines of QSCCs and PCCs with lifetimes are less than or equal to 90 minutes seems to follow a certain line in the diagram, which suggests that there should be a scale similarity in terms of the lifetime.

## 3.2   Rainfall characteristics

After classifying QSCCs and PCCs, we estimate the rainfall amounts due to these CCs. In addition, the

Table 1.  The types of rainfall characteristics used in this study. P, S, V means precipitation intensity, precipitating area, and lifetime averaged motion speed, respectively.

| Type | $P \geq 10$ mm h$^{-1}$ | $S \geq 200$ km$^2$ | $V \geq 10$ m s$^{-1}$ | $V < 10$ m s$^{-1}$ |
|------|------------------------|---------------------|------------------------|---------------------|
| A | – | N | – | – |
| B | Y | N | – | – |
| C (QSCC) | Y | Y | N | Y |
| D (PCC) | Y | Y | Y | N |
| E (SLCC) | Y | Y | Lifetime < 20 min | |

total rainfall amounts are divided into categories that will comprehensively demonstrate the rainfall characteristics during the heavy rainfall events of 2017 and 2018. In this subsection, we examine the fractions of the rainfall amounts due to QSCCs, PCCs, and other types of precipitating events.

We divided the rainfall intensity in the radar data at each time step into five rainfall types. First, we defined rainfall intensities of greater than or equal to 0.05 mm h$^{-1}$ and less than 10 mm h$^{-1}$ as weaker rainfall (Type A). Rainfall intensities of greater than or equal to 10 mm h$^{-1}$ (which are regarded as convective rainfall) are divided into the following four types. If the contiguous area of convective rainfall is less than 200 km$^2$, it is defined as an unorganized rainfall system (Type B). If the contiguous area of the rainfall is greater than or equal to 200 km$^2$, it is defined as being produced either by a QSCC (Type C), PCC (Type D), or SLCC (Type E). Rainfall with a lifetime shorter than 20 minutes is categorized as being produced by an SLCC because of the lifetime limitation described in Section 3.1. All the rainfall types used in this study are summarized in Table 1.

Figure 7 shows the horizontal distributions of the contribution from each rainfall type to the total rainfall amount in each 1 km by 1 km area during the 2017 case. Type A rainfall is dominant over the analysis area, indicating that its rainfall contribution exceeds 80 % (Fig. 7a). In regions where a large amount of the total rainfall occurred, including the northern part of Kyushu (see Fig. 2a), the Type A contribution is less than 50 %. Stronger rains with intensities exceeding 10 mm h$^{-1}$ are divided into four types (B–E). The Type B rainfall contribution is less than 10 % (Fig. 7b), whereas the contributions from Types C and D are greater than 20 % (Figs. 7c, d). Fig. 7e shows regions with Type E rainfall contributions exceeding 20 %, which correspond to the areas with a lower percentage of Type A rainfall.

In the 2018 case (Fig. 8), the rainfall contribution features are the same as those seen in the 2017 case.

In regions where a large amount of rainfall occurred, such as the western and central parts of Japan as shown in Fig. 2b, the percentage of rainfall contribution from Type A is less than 60 %. In these regions, the contribution from Type E is greater than 30 %. Although the Type C rainfall contribution is smaller than 10 %, that from Type D is greater than 20 %.

Here we summarize the common/different features found in the 2017 and 2018 cases. Rainfall amounts attributable to the weaker type (i.e., Type A) contribute dominantly to the total rainfall in most of the regions; however the contribution from stronger rains become larger in the heaviest rainfall regions. Among the stronger types, SLCCs dominate over rainfall contributions from QSCCs or PCCs. There are some regions (e.g., Shikoku Island) where QSCC and PCC rainfall contributions from QSCCs in the 2017 case and PCCs in the 2018 case were major players in producing the total rainfall. SLCC rainfall is produced by organized but short-lived precipitating systems. In contrast, ranfall amounts from unorganized systems (Type B) is very minor. Thus, the contribution from stronger rains is mainly due to organized systems (Types C, D, and E) in regions with significant rainfall amounts.

In the next section, we investigate how environmental conditions characterize the types of rainfall categorized in this section.

## 4.  Environmental properties of the rainfall types

We examined the properties of the environmental conditions for the occurrence of each rainfall type using MA data. The procedure to define the environmental conditions is explained as follows.

To determine each rainfall type's environmental properties, we first located the points of detected QSCCs and PCCs. We then defined the environmental values for a QSCC or PCC as the spatial means of the CC averaged over a 100 km$^2$ area centered at the QSCC or PCC centroid within 3 hours before the QSCC or PCC was first detected in the time series at each point. Thus, the environmental conditions were
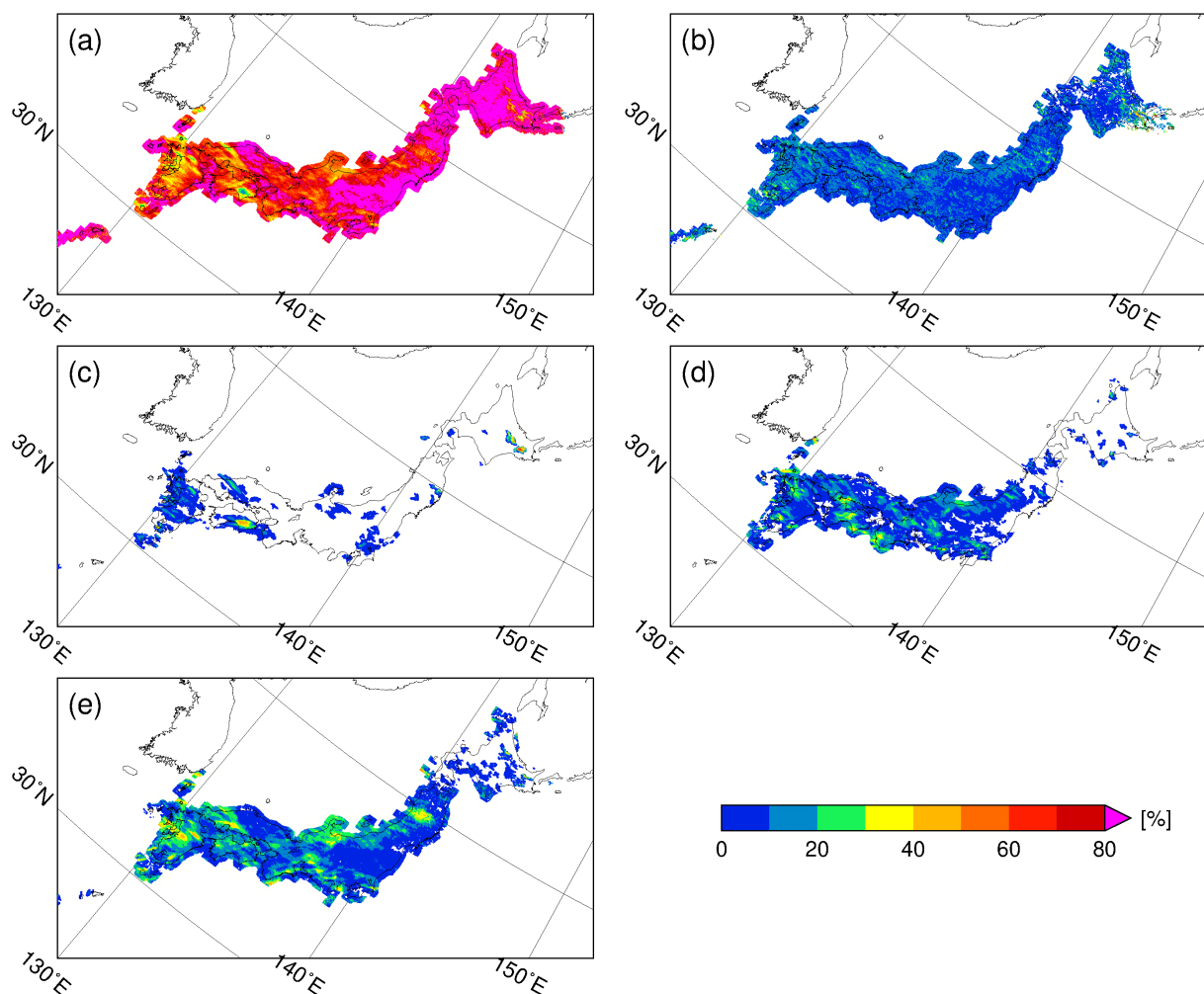
Fig. 7.    Contributions of rainfall Types A−E against total rainfall during the 2017 case: (a) Type A rainfall with precipitation intensity less than 10 mm h$^{-1}$, (b) Type B rainfall with precipitation intensity greater than or equal to 10 mm h$^{-1}$ and precipitating area less than 200 km$^2$, (c) Type C rainfall with precipitation intensity greater than or equal to 10 mm h$^{-1}$ and precipitating area greater than or equal to 200 km$^2$ and with lifetime-averaged motion speed of convective clusters being less than 10 m s$^{-1}$ and lifetime greater than or equal to 20 minutes, (d) Type D rainfall, which is as (c), but with lifetime-averaged motion speed greater than 10 m s$^{-1}$, and (e) other convective clusters (Type E).

defined as the spatially averaged states prior to the occurrence of QSCCs or PCCs. Next, we examined the rainfall types at a QSCC or PCC location in a time series that traced back and forth from the time when the QSCC or PCC was detected. If Types A, B, and E were detected in this time series, the environmental conditions were then defined as the spatially averaged fields computed from the MA data at the nearest time before a QSCC or PCC was detected. A difference in defining the environments for Types A, B, and E arises from differences in the location for evaluating each type's environment, depending on the time for each type to be detected. The environmental conditions for the development of the QSCCs in UT16a depended highly on the location of an upper-air observation site to determine the QSCC environment. However, there is no such limitation for determining locations of the environments for the rainfall types in this study because of the use of MA grid data. Thus, the present analysis can define the environmental conditions for the development of Types A, B, and E based on the detected locations of QSCCs or PCCs.
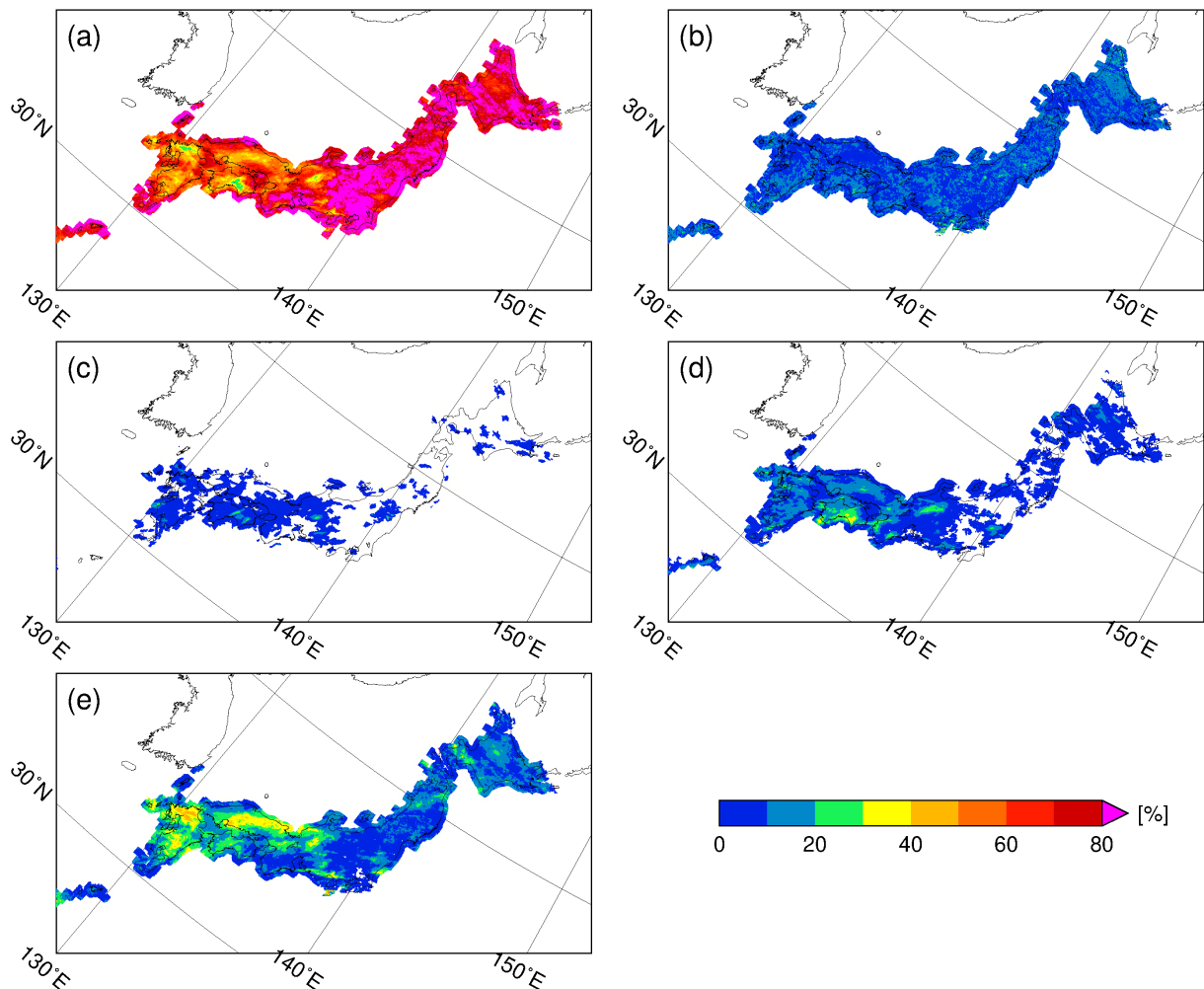
Fig. 8.    The same as Fig. 7, except for the 2018 case.

### 4.1    Vertical profiles

Before examining the MA data, we checked the quality of the MA data used in this study by comparing them with upper-air sonde observation data. Supplements 1 and 2 summarize the comparisons between the MA data and sonde data in terms of temperature, relative humidity, and zonal and meridional winds at 925, 850, 700, and 500 hPa at Wakkanai, Sapporo, Akita, Wajima, Tateno, Matsue, Shionomisaki, Fukuoka, and Kagoshima during the analysis periods in this study. The MA data are spatially averaged over a 100 km² area centered at the sounding site. The correlation coefficients for temperature are generally greater than 0.8, whereas those for relative humidity exceed 0.7. The coefficients for zonal and meridional wind mostly have values greater than 0.9. Although

relative humidity of the MA data seems to have some bias against observations, the MA data are considered to represent actual atmospheric conditions, especially over land and in surrounding coastal areas.

The vertical profiles of temperature, relative humidity, and zonal and meridional winds for each rainfall type are shown in Figs. 9 and 10 for the 2017 and 2018 cases, respectively (see Supplements 4 and 5 for more details). The temperature profiles in both years show no salient difference among the rainfall types (Figs. 9a, 10a), except in the lower and upper troposphere in 2018. As for relative humidity (Figs. 9b, 10b), a common feature between the 2017 and 2018 cases is that the relative humidity of Type A (Type D) is drier (moister) throughout the troposphere than that of other types. It appears that there are not any
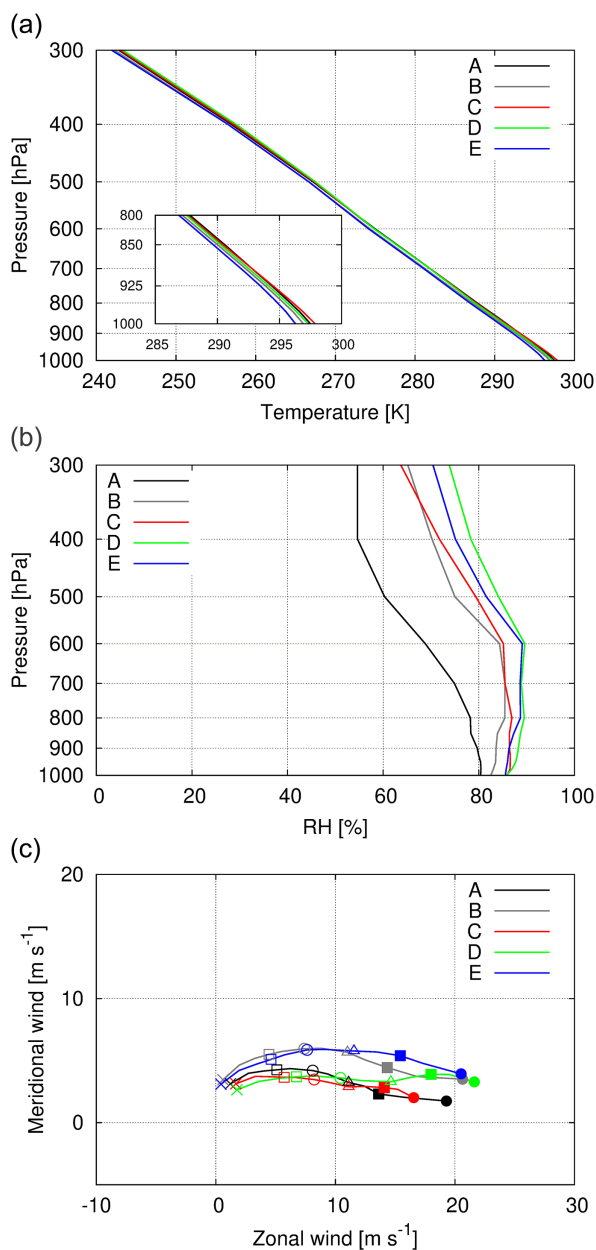
Fig. 9. Vertical profile of (a) temperature, (b) relative humidity, and (c) zonal and meridional winds averaged from JMA's mesoscale analysis data within a 100 km² area for rainfall Types A−E for the 2017 case. In (c), crosses, rectangles, circles, triangles, filled rectangles, and filled circles represent 1000, 925, 850, 700, 500, and 300 hPa, respectively.
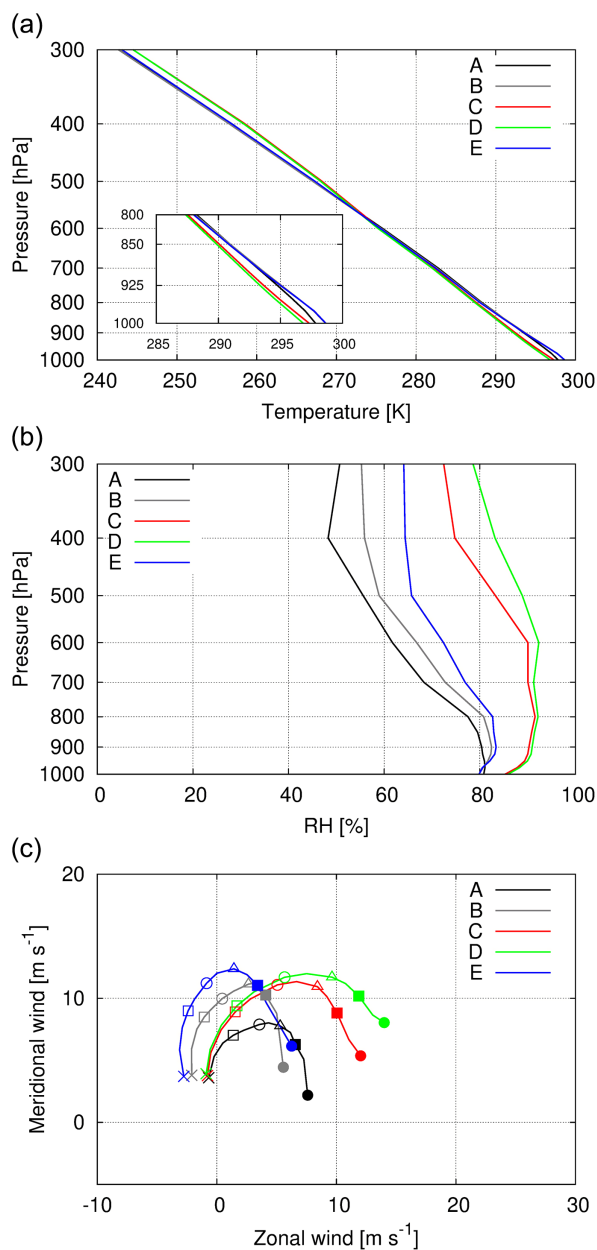
Fig. 10. The same as Fig. 9, except for the 2018 case.

common features in Types B, C, and E between the 2017 and 2018 cases. However, a clear feature is that relative humidity differences among the rainfall types is more enhanced in 2018 than in 2017.

The wind hodographs (Figs. 9c, 10c) indicate that westerly winds are generally dominant in the 2017 case whereas veering wind dominates in the 2018 case. This clear difference in shear between the 2017
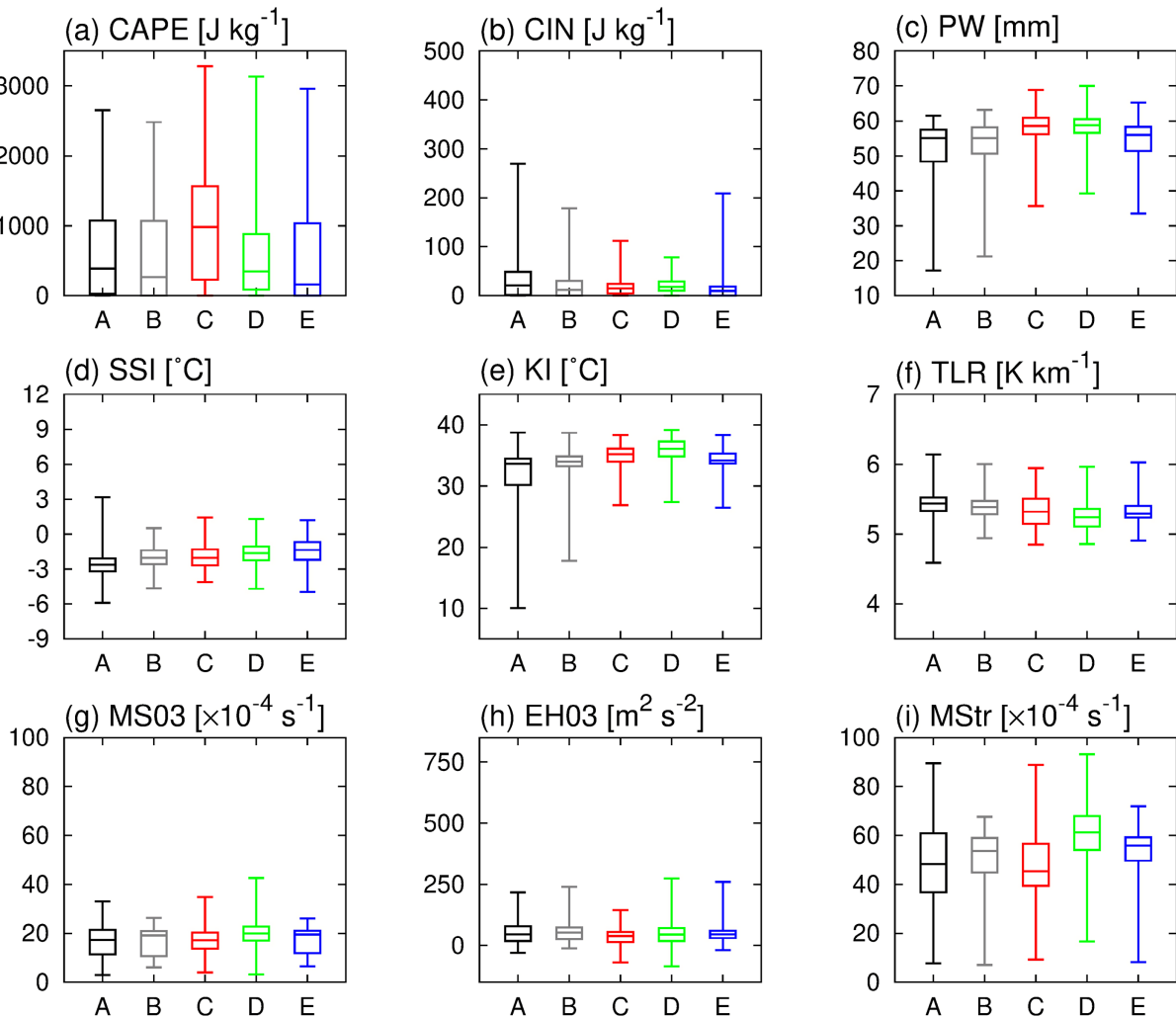
Fig. 11.   Box-and-whisker plots of the environmental parameters calculated from JMA mesoscale analysis data for rainfall Types A–E in the 2017 case: (a) CAPE (J kg$^{-1}$), (b) CIN (J kg$^{-1}$), (c) PW (mm), (d) SSI (°C), (e) KI (°C), (f) TLR (K km$^{-1}$), (g) MS03 (× 10$^{-4}$ s$^{-1}$), (h) EH03 (m$^2$ s$^{-2}$), and (i) MStr (× 10$^{-4}$ s$^{-1}$). The whiskers at the upper and lower ends represent the maximum and minimum values, respectively, and the middle line in each box indicates the median. The top and bottom lines of each box indicate the 75 and 25 percentiles, respectively. The values are averaged over each 100 km$^2$ area.

and 2018 cases is considered to characterize the shape and propagating natures of CCs and rainfall types. The 2018 case shows that the shear magnitude is a little stronger in Type D than in Type C, which is reasonable because Type D rainfall is produced by propagating systems. The features of shear will be further examined in the following analysis in terms of shear-related parameters.

### 4.2   Environmental indices

As explained in Section 2, the characteristics of

stability and vertical shear are diagnosed in terms of environmental indices and parameters.

Box-and-whisker plots of the environmental parameters examined here for all rainfall types in the 2017 case are shown in Fig. 11. The distributions of the parameters related to static stability (Figs. 11a–f) demonstrate that Type A shows more occurrences of larger CIN, smaller PW, and smaller KI than the other types, and that Types C and D show more occurrences of larger PW and larger KI than the other types. In contrast, the parameters related to vertical shear (Figs.
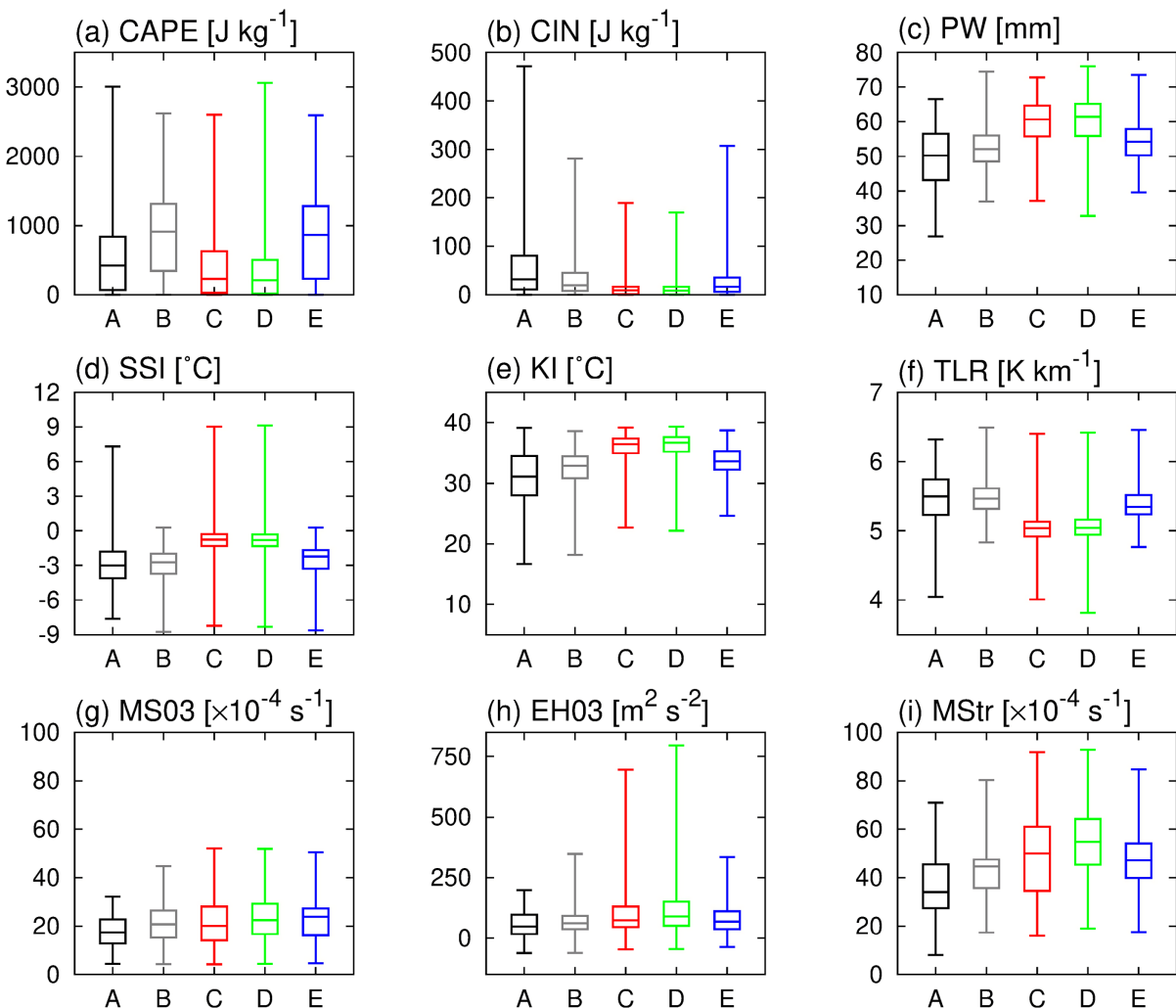
Fig. 12.   The same as Fig. 11, except for the 2018 case.

11g–i) demonstrate that Type C rainfall shows smaller magnitudes than the other rainfall types for MS03 and MStr and Type D rainfall clearly shows larger magnitudes of MStr. Because all the rainfall types dominantly show westerly winds, EH03 does not change significantly among them.

The environmental conditions for the 2018 case are shown in Fig. 12. As in Fig. 11, Type A has greater frequencies of larger CIN, smaller PW, and smaller KI than the other types, whereas Types C and D show more occurrences of larger PW and larger KI than the others. In addition, there are some differences in the shear parameters among the rainfall types. Type C shows nearly the same MS03 value among the types, but it has a larger MStr than the other types except for

Type D in the 2018 case. Because of veering winds, EH03 in 2018 appears to have in general larger than that in 2017.

By comparing the distributions of the 2017 and 2018 cases we find that PW is larger in the 2018 case than in the 2017 case overall. Because of this larger amount of moisture in 2018, KI also seems to be larger in 2018. Thus, conditions are more unstable in 2018 than in 2017 in terms of moisture content. Furthermore, in both years MStr appears to distinguish the environmental conditions for the rainfall types rather than MS03 because the lower-level shear is similar among the types as seen in Figs. 9c and 10c.

We used PW and MStr from the above analysis to examine how temporal changes of the environmental
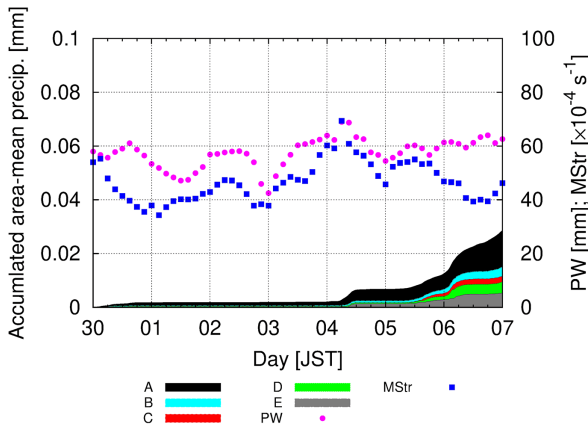
Fig. 13.  Time series of accumulated 50 km² area-averaged precipitation for rainfall Types A–E in the Fukuoka region in the 2017 case. The 100 km² area-averaged values of PW and MStr are also drawn as magenta circles.



Fig. 14.  The same as Fig. 13, except for the Ehime region in the 2018 case.

conditions characterize the development of each rainfall type. In the following, we focused on a specific area for each year. For the 2017 case we chose the area corresponding to a Fukuoka region in which heavy rainfall occurred and several QSCCs and PCCs were detected. For the 2018 case we chose an area corresponding to an Ehime region where multiple QSCCs developed. These regions are at almost the same latitude and have relatively similar climatic characteristics. Therefore, the Fukuoka and Ehime regions are adequate for comparing the environmental properties for rainfall system development to compare rainfall features with different spatiotemporal scales between the 2017 and 2018 cases under an identical analysis method.

The temporal changes of PW and MStr and the accumulated area-mean rainfall amount by each type for the 2017 case are shown in Fig. 13. From 30 June to 4 July, Type A rainfall develops and is dominant, with some developments of Types B and E. The contribution from the Type B rainfall is very minor, as can be seen in Fig. 7b. During this period, PW varies between 50 mm and 60 mm, and increases to more than 60 mm on 4 July. On 5 July, when the heavy rainfall occurred in the Fukuoka region, Types C, D, and E develop, and the rainfall contribution from these types becomes large. In particular, the total contributions from Types C, D, and E reach and exceed 0.5. MStr varies similarly to PW, indicating some variations from 30 June to 3 July, and shows an increasing trend on 3 and 4 July. After this period, Types C, D, and E develop. Note
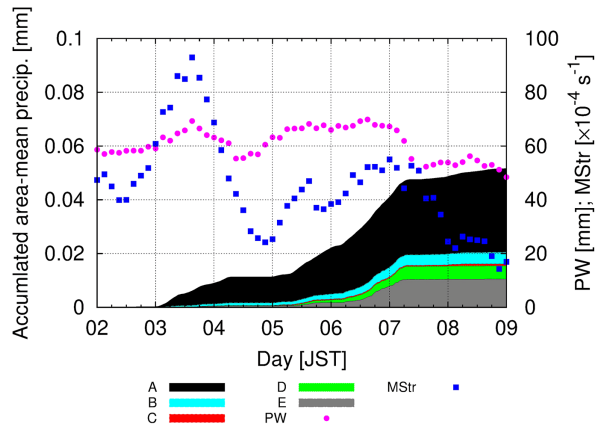
that Type C occurs after MStr decreases on July 5.

Figure 14 shows the temporal changes of the rainfall types, PW, and MStr for the Ehime region in the 2018 case. Type A rainfall is dominant, and Type B and E appear subsequently. The contribution from Type E becomes more continuous after 6 July. At the same time, Types C and D are activated. PW values are greater than 60 mm from 2 to 6 July, and these PW values are higher than those in the 2017 case. PW becomes large as Type A activity increases on 3 and 5–6 July. After the activation of Type E, Type C rainfall appears on 8 July.

In summary, the temporal changes of rainfall types and environmental properties (i.e., PW and MStr) demonstrate that the Type E rainfall develops concurrently with increases in PW and MStr. Type A rainfall continuously develops throughout the analysis time periods, including when PW is relatively small. These features in the time series appear in the frequency distributions shown in Figs. 11 and 12. In this way, the rainfall types seem to develop in relation to variations in PW, MS03, and MStr.

## 5.  Discussion

Characteristics of rainfall and the environmental conditions for rainfall occurrence during the heavy rainfall events of July 2017 and 2018 were investigated with the use of precipitation radar data and mesoscale analysis data. In this section, we interpret the results from the data analyses.

The algorithm to detect QSCCs, which was developed by UT16a from the original algorithm of Shimizu and Uyeda (2012), was extended to identify

PCCs (i.e., faster-moving CCs) in addition to QSCCs. We then classified rainfalls based on rain intensity and rain area into five types (Types A–E), which included rainfall produced by QSCCs and PCCs. The rainfall type categories included weaker rainfall (Type A), convective but unorganized rainfall (Type B), QSCC rainfall (Type C), PCC rainfall (Type D), and SLCC rainfall (Type E). The contribution from convective types (Types B–E) became dominant in regions where heavy rainfall occurred. Among the convective rainfall types, Type E had the largest contribution. UT16a showed that QSCC rainfall's contribution to the total rainfall during the warm season throughout Japan accounts for at most 5 % or so. The present analyses demonstrated the QSCC and PCC rainfalls had contributions of around 20 %, which is larger than that found in UT16a. This is because of the increase in the number of QSCC detections by the revised version of the UT16a algorithm. Although the present algorithm may require some updates in a future study to fully cover QSCCs and PCCs by decreasing the number of SLCCs (Type E) identified, the present analysis successfully indicated that the rainfall contribution from convective systems with areas exceeding 200 km$^2$ played a major part in producing heavy rainfalls.

The environmental analyses indicated that relative humidity, moisture content (PW), and vertical shear (MS03 and MStr) are more effective in distinguishing rainfall types than other environmental parameters. Because of differences in PW, the parameters such as CIN and KI seem to somewhat distinguish the environmental properties of the rainfall type. Compared with the statistical analysis by UT16a, the PW values in the 2017 case are very similar to the statistical mean whereas those in the 2018 case include statistically higher ranges. The vertical shear in both the 2017 and 2018 cases includes higher ranges. UT16a demonstrated that the environment of faster-moving QSCCs, which have motion speed of 7.4–10 m s$^{-1}$, has a stronger vertical shear than that of slower-moving QSCCs, which have motion speed of 0–3.8 m s$^{-1}$. In the present analysis, vertical shear was shown to be stronger in Types D and E than in Type C. This result is consistent with the statistical analysis by UT16a; therefore, vertical shear is shown to play a role in determining the stationary or propagating characteristics of CCs.

We examined environmental conditions in areas where QSCCs or PCCs were detected. As shown in Figs. 4 and 5, the locations of QSCC or PCC occurrences were not distributed throughout the Japanese islands, and the locations were not the same in the

2017 and 2018 cases. Thus, the properties revealed by the present analysis may be affected by location choices. The reason we focused on areas where QSCCs or PCCs occurred is that the environmental properties can be directly compared with the statistical analysis presented by UT16a. The analysis by UT16a can be regarded as a baseline for diagnosing environmental conditions for the occurrence of organized CCs. This is because there are no other studies examining the statistical properties of mesoscale convective systems over Japan. Chuda and Niino (2005) investigated the mesoscale background properties of atmospheric conditions; however, their analysis covered data that included both precipitation events and fair-weather conditions. Thus, the statistics of UT16a are considered to be the baseline for comparing the environmental conditions of different rainfall types with the statistical characteristics of the environment. More careful procedures to identify mesoscale convective systems with an updated automatic algorithm based on UT16a are expected to provide more robust definitions of the environmental conditions for the development of mesoscale convective systems.

## 6. Conclusions

This study investigated the characteristics of rainfall types and the environmental conditions for the development of the heavy rainfall events over Japan in July of 2017 and 2018. Operational precipitation radar data were used to examine the rainfall characteristics and the analysis fields from the JMA MSM were used to identify the environmental conditions for the heavy rainfall events. We applied and extended the algorithm of UT16a to separate QSCCs, PCCs, and SLCCs. With this automatic detection algorithm, we categorized rainfall characteristics into five types: weaker rainfall (Type A), convective but unorganized rainfall (Type B), QSCC rainfall (Type C), PCC rainfall (Type D), and SLCC rainfall (Type E). We then examined the environmental conditions for these rainfall types.

Although the Type A rainfall has the largest contribution to the total amount of rainfall over most of the areas in Japan in the 2017 and 2018 cases, the contribution from the convective types (Types B–E) became dominant in regions where heavy rainfall occurred. Among the convective types, Type E has the greatest contribution and Type B has the smallest contribution. The contributions from the Type C and Type D rainfalls (i.e., from QSCCs and PCCs) were found to be relatively small, which is likely due to some deficiencies in capturing convective systems with the automatic algorithm of UT16a despite improvements

made in this study. However, it is emphasized that organized convective systems with areas of 200 km$^2$ or larger played a major role in generating heavy rainfall during the events in July of 2017 and 2018.

The analyses of the environmental conditions demonstrated that middle-to-upper-level relative humidity, PW, MS03, and MStr more effectively distinguished the environmental conditions for the present rainfall types better than other environmental parameters. It is important to recognize that both PW and relative humidity at middle-to-upper levels characterize the environmental conditions for the occurrence of the heavy rainfall events examined here. Compared with the statistical analysis by UT16a, the PW value of the 2017 case is very similar to the statistical mean whereas that of the 2018 case includes statistically higher values. Both MStr and MS03 were shown to be stronger in Type D rainfall than in Type C rainfall. This indicates that vertical shear plays a role in determining the stationary or propagating characteristics of CCs.

The analyses of temporal changes of rainfall types and environmental properties indicated that Type E rainfall develops at the same time as PW and MStr increase, whereas Type C rainfall occurs when MStr is relatively weak. Type A rainfall continuously develops throughout the analysis time periods, even when PW is relatively small. The rainfall types were thus shown to develop in relation to the variations of moisture content and vertical shear.

Some future developments and studies were also discussed. Because of the diversity and complexity of mesoscale convective systems, defining and extracting the features of rain-producing cloud systems are difficult tasks. In response to the significant disasters resulting from the heavy rainfall events in July of 2017 and 2018, we should further advance the current automatic algorithm to precisely detect convective systems from operational radar data and use that updated algorithm for operational purposes. With more sophisticated advances, an updated algorithm could be used in monitoring and now-casting the development of mesoscale convective systems.

## Supplements

Supplement 1 compares temperature, relative humidity, and horizontal wind speeds between the MA data and radiosonde data at observation sites during the 2017 case analysis period.

Supplement 2 is the same as Supplement 1, but for the 2018 case.

Supplement 3 shows the accumulated rainfall amounts for the original 1 km resolution data (a) from 0000 JST 30 June to 0000 JST 7 July 2017 and (b) from 0000 JST 2 July to 0000 JST 9 July 2018.

Supplement 4 shows the vertical profile of temperature, relative humidity, and zonal and meridional winds averaged from MA grid data within a 100 km$^2$ area with box-and-whisker plots for rainfall Types A−E for the 2017 case.

Supplement 5 is the same as Supplement 4, but for the 2018 case.

## Acknowledgments

## References

Cabinet Office, 2019: *A report on damages by the July 2018 Heavy Rainfall*. The version of 1 January 2019, 204 pp (in Japanese). [Available at http://www.bousai.go. jp/updates/h30typhoon7/pdf/310109_1700_h30typhoon 7_01.pdf.]

Chuda, T., and H. Niino, 2005: Climatology of environmental parameters for mesoscale convections in Japan. *J. Meteor. Soc. Japan*, **83**, 391–408.

Davies-Jones, R., 1984: Streamwise vorticity: The origin of updraft rotation in supercell storms. *J. Atmos. Sci.*, **41**, 2991–3006.

Derbyshire, S. H., I. Beau, P. Bechtold, J.-Y. Grandpeix, J.-M. Piriou, J.-L. Redelsperger, and P. M. M. Soares, 2004: Sensitivity of moist convection to environmental humidity. *Quart. J. Roy. Meteor. Soc.*, **130**, 3055–3079.

George, J. J., 1960: *Weather Forecasting for Aeronautics*. Academic Press, New York, 673 pp.

Hamada, A., and Y. N. Takayabu, 2018: Large-scale environmental conditions related to midsummer extreme rainfall events around Japan in the TRMM region. *J. Climate*, **31**, 6933–6945.

Japan Meteorological Agency, 2013: *Outline of the operational numerical weather prediction at the Japan Meteorological Agency*. Japan Meteorological Agency, 201 pp. [Available at https://www.jma.go.jp/jma/jma-eng/jma-center/nwp/outline2013-nwp/index.htm.]

Kato, R., K. Shimose, and S. Shimizu, 2018: Predictability of precipitation caused by linear precipitation systems during the July 2017 Northern Kyushu heavy rainfall event using a cloud-resolving numerical weather prediction model. *J. Disaster Res.*, **13**, 846–859.

Kikuchi, K., and Y. N. Takayabu, 2004: The development of organized convection associated with the MJO during TOGA COARE IOP: Trimodal characteristics. *Geophys. Res. Lett.*, **31**, L10101, doi:10.1029/2004GL 019601.

Nagata, K., 2011: Quantitative precipitation estimation and quantitative precipitation forecasting by the Japan Meteorological Agency. *RSMC Tokyo–Typhoon Center Technical Review*, **13**, 37–50. [Available at https://www.jma.go.jp/jma/jma-eng/jma-center/rsmc-hp-pub-eg/techrev/text13-2.pdf.]

Nomura, S., and T. Takemi, 2011: Environmental stability for afternoon rain events in the Kanto Plain in summer. *SOLA*, **7**, 9–12.

Rasmussen, E. N., and D. O. Blanchard, 1998: A baseline climatology of sounding-derived supercell and tornado forecast parameters. *Wea. Forecasting*, **13**, 1148–1164.

Saito, K., T. Fujita, Y. Yamada, J.-i. Ishida, Y. Kumagai, K. Aranami, S. Ohmori, R. Nagasawa, S. Kumagai, C. Muroi, T. Kato, H. Eito, and Y. Yamazaki, 2006: The operational JMA nonhydrostatic mesoscale model. *Mon. Wea. Rev.*, **134**, 1266–1298.

Sekizawa, S., T. Miyasaka, H. Nakamura, A. Shimpo, K. Takemura, and S. Maeda, 2019: Anomalous moisture transport and oceanic evaporation during a torrential rainfall event over western Japan in early July 2018. *SOLA*, **15A**, 25–30.

Shimizu, S., and H. Uyeda, 2012: Algorithm for the identification and tracking of convective cells based on constant and adaptive threshold methods using a new cell-merging and -splitting scheme. *J. Meteor. Soc. Japan*, **90**, 869–889.

Shimpo, A., K. Takemura, S. Wakamatsu, H. Togawa, Y. Mochizuki, M. Takekawa, S. Tanaka, K. Yamashita, S. Maeda, R. Kurora, H. Murai, N. Kitabatake, H. Tsuguti, H. Mukougawa, T. Iwasaki, R. Kawamura, M. Kimoto, I. Takayabu, Y. N. Takayabu, Y. Tanimoto, T. Hirooka, Y. Masumoto, M. Watanabe, K. Tsuboki, and H. Nakamura, 2019: Primary factors behind the heavy rain event of July 2018 and the subsequent heat wave in Japan. *SOLA*, **15A**, 13–18.

Sueki, K., and Y. Kajikawa, 2019: Different precipitation systems between Hiroshima and Keihanshin during extreme rainfall event in western Japan in July 2018. *J. Meteor. Soc. Japan*, **97**, 1221–1232.

Takemi, T., 2006: Impacts of moisture profile on the evolution and organization of midlatitude squall lines under various shear conditions. *Atmos. Res.*, **82**, 37–54.

Takemi, T., 2007a: A sensitivity of squall-line intensity to environmental static stability under various shear and moisture conditions. *Atmos. Res.*, **84**, 374–389.

Takemi, T., 2007b: Environmental stability control of the intensity of squall lines under low-level shear conditions. *J. Geophys. Res.*, **112**, D24110, doi:10.1029/2007JD008793.

Takemi, T., 2010: Dependence of the precipitation intensity in mesoscale convective systems to temperature lapse rate. *Atmos. Res.*, **96**, 273–285.

Takemi, T., 2014a: Characteristics of summertime afternoon rainfall and its environmental conditions in and around the Nobi Plain. *SOLA*, **10**, 158–162.

Takemi, T., 2014b: Convection and precipitation under various stability and shear conditions: Squall lines in tropical versus midlatitude environment. *Atmos. Res.*, **142**, 111–123.

Takemi, T., 2015: Relationship between cumulus activity and environmental moisture during the CINDY2011/DYNAMO field experiment as revealed from convection-resolving simulations. *J. Meteor. Soc. Japan*, **93A**, 41–58.

Takemi, T., 2018: Importance of terrain representation in simulating a stationary convective system for the July 2017 northern Kyushu heavy rainfall case. *SOLA*, **14**, 153–158.

Takemi, T., and T. Unuma, 2019: Diagnosing environmental properties of the July 2018 heavy rainfall event in Japan. *SOLA*, **15A**, 60–65.

Takemi, T., and T. Unuma, 2020: Environmental factors for the development of heavy rainfall in the eastern part of Japan during Typhoon Hagibis (2019). *SOLA*, **16**, 30–36.

Takemi, T., O. Hirayama, and C. Liu, 2004: Factors responsible for the vertical development of tropical oceanic cumulus convection. *Geophys. Res. Lett.*, **31**, L11109, doi:10.1029/2004GL020225.

Takemura, K., S. Wakamatsu, H. Togawa, A. Shimpo, C. Kobayashi, S. Maeda, and H. Nakamura, 2019: Extreme moisture flux convergence over western Japan during the heavy rain event of July 2018. *SOLA*, **15A**, 49–54.

Tsuguti, H., and T. Kato, 2014: Objective extraction of heavy rainfall events and statistical analysis on their characteristic features. *Tenki*, **61**, 455–469 (in Japanese).

Tsuguti, H., N. Seino, H. Kawase, Y. Imada, T. Nakaegawa, and I. Takayabu, 2019: Meteorological overview and mesoscale characteristics of the heavy rain event of July 2018 in Japan. *Landslides*, **16**, 363–371.

Unuma, T., and T. Takemi, 2016a: Characteristics and environmental conditions of quasi-stationary convective clusters during the warm season in Japan. *Quart. J. Royal Meteor. Soc.*, **142**, 1232–1249.

Unuma, T., and T. Takemi, 2016b: A role of environmental shear on the organization mode of quasi-stationary convective clusters during the warm season in Japan. *SOLA*, **12**, 111–115.

Yokoyama, C., Y. N. Takayabu, and T. Horinouchi, 2017: Precipitation characteristics over East Asia in early summer: Effects of the subtropical jet and lower-tropospheric convective instability. *J. Climate*, **30**, 8127–8147.